



Microstructural design for enhanced shape memory behavior of 4D printed composites based on carbon nanotube/poly(lactic acid) filament

Yang Liu^{a,b}, Wei Zhang^a, Fenghua Zhang^c, Jinsong Leng^c, Shaopeng Pei^b, Liyun Wang^b, Xinqiao Jia^d, Chase Cotton^e, Baozhong Sun^a, Tsu-Wei Chou^{b,*}

^a College of Textiles, Donghua University, Shanghai, 201620, PR China

^b Department of Mechanical Engineering, University of Delaware, Newark, DE, 19716, USA

^c Center for Composite Materials and Structures, Harbin Institute of Technology, Harbin, 150080, PR China

^d Department of Materials Science and Engineering, University of Delaware, Newark, DE, 19716, USA

^e Department of Electrical and Computer Engineering, University of Delaware, Newark, DE, 19716, USA

ARTICLE INFO

Keywords:

4D printing
Carbon nanotube
Angle-ply laminated preform
Rectangular braided preform
Shape memory property

ABSTRACT

Four-dimensional (4D) printing technology, combining 3D printing with stimuli-responsive materials, has attracted extensive attention for smart additive manufacturing. This work focuses on microstructural design, shape recovery behavior and recovery force characterization of 4D printed angle-ply laminated and rectangular braided preforms and their silicone elastomer matrix composites. The angle-ply laminated and rectangular braided preforms were printed using poly(lactic acid) (PLA) and carbon nanotube reinforced PLA (CNT/PLA) based shape memory polymer (SMP) filaments. The X-ray micro-computed tomography, a high resolution and nondestructive imaging technique, was employed to characterize the microstructures of 4D printed specimens and their post-bending damage morphology. The effects of microstructure, CNT filler and silicone elastomer matrix on shape recovery behavior, recovery force and flexural property were studied. The infilling of CNT enabled earlier initiation of specimen shape recovery process, improved the recovery force up to 144% and enhanced the flexural load and modulus. The infusion of silicone matrix increased the final shape recovery ratio to 97.3%, improved the recovery force and enhanced flexural property. The knowledge gained in this research will benefit future design optimization for smarter, faster and stronger actuators.

1. Introduction

Three-dimensional (3D) printing technology, also termed additive manufacturing, has been rapidly developed and widely applied in many manufacturing fields due to the minimization in material waste and the capability of fabricating objects of complex shape from micro- to macro-scale [1,2]. 3D printing techniques have been under rapid development for nearly three decades and there are currently over 50 different additive manufacturing techniques, such as fused deposition modeling (FDM), direct ink writing (DIW), stereolithography (SLA), etc [2]. Materials used in the conventional 3D printing are mainly non-active materials whose shape and function are mostly fixed [3]. Stimuli-responsive materials, on the other hand, can change shape, property and function under a certain stimulus, such as heat, light, electricity, magnetism, water and chemical [4,5]. Four dimensional (4D) printing, first introduced by Tibbitts [6], utilizes stimuli-responsive materials to add the time-dimension to 3D printing of devices which exhibit shape-

property- and function-change over time [7,8]. Owing to the rapid growth and interdisciplinary research of 3D printing and stimuli-responsive materials, 4D printing has demonstrated its tremendous potential in many engineering applications, such as robotics [9], origami based actuators [10–12], adaptive metamaterials [13,14], drug delivery [15] and fashionwear [16].

Several methods have been adopted to achieve 4D printing. For example, the simplest approach to realize 4D printing is by combining 3D printing with one of the stimuli-responsive materials, which mostly include shape memory polymer (SMP) [17–20], hydrogel [21,22] and liquid crystal elastomers [23,24]. Next, the release of residual stress, which was created in the printing process, under heat treatment can be utilized to induce shape-change [13,25–27]. Thirdly, a structure printed with property-mismatched (i.e., modulus and coefficient of thermal expansion) multi-materials can undergo a complex shape-shifting under a certain stimulus [28–30]. These above research efforts mainly focus on the realization of shape-changes of the printed objects.

* Corresponding author.

E-mail address: chou@udel.edu (T.-W. Chou).

<https://doi.org/10.1016/j.compscitech.2019.107692>

Received 17 January 2019; Received in revised form 12 June 2019; Accepted 15 June 2019

Available online 18 June 2019

0266-3538/ © 2019 Elsevier Ltd. All rights reserved.

Among the stimuli-responsive materials, SMP has been extensively used and developed in 4D printing technology [7,31]. Furthermore, shape recovery ratio and recovery force are considered as the key parameters of shape recovery capacity of a 4D printed structure. In order to improve shape recovery capacity of SMP, Chen and Shea [32] designed a force-amplified structure to achieve larger recovery force. Akbari et al. [33] printed elastomer hinges for assisting the SMP structure in achieving larger recovery force. Furthermore, significant efforts have also been made by researcher in achieving high shape recovery capacity of SMP composites by using reinforcing fillers, such as graphite oxide [34], carbon nanotube (CNT) [35], carbon fiber [36], TiO₂ particle [37], etc. However, there seems to be a lack of study on shape recovery capacity of 4D printed nano-filler reinforced SMP lightweight functional composites. Lastly, it should be noted that although most of the existing research has focused on the characterization of recovery force subjected to tensile load [38–40], in the majority of applications of 4D printed structures as sensors and actuators, bending loads are more prevalent.

A major focus of our current research in 3D printing is the development of functional composites for applications in sensors and actuators. To this end, a two-prone approach has been adopted, namely, microstructural design and materials research of the preforms and their composites. In preform microstructural design, particular attention was devoted to conventional laminated preforms as well as 3D textile preforms. For instance, the works of Quan et al. [1,41,42] and Zhang et al. [43,44], have demonstrated the enormous potential of microstructural design and fabrication of preforms based on 3D printing and fused deposition modeling, as well as the residual stress and deformation in 3D printed preforms and their composites. In functional applications as sensors and actuators, Zhang et al. [45] and Liu et al. [12] have examined the basic subject of recovery force generated by 4D printed preforms and their composites. In order to further broaden our understanding of the above two outlined research objectives, a preliminary study in the optimization of microstructural design using angle-ply laminated preform and braided preform has been carried out. Here, we report the effort in comparing the effectiveness in shape recovery ratio and recovery force of 4D printed angle-ply laminated preform and braided preform using PLA and CNT/PLA SMP filaments. The 3D models of the angle-ply laminated and braided preforms with the same yarn orientation (45°) and volume fraction (38%) were designed. Besides, the preforms were also infused with silicone elastomer matrix for better shape recovery capacity. Recovery force of 4D printed specimens was measured using DMA 3-point bending mode. Flexural property of 4D printed specimens was characterized using 3-point bending test. Finally, the microstructure of as-printed preforms and the damage morphology of post-bending specimens were examined using X-ray micro-computed tomography imaging.

2. Material and experimental characterization

2.1. Filament material and its thermal property characterization

The carbon nanotube (CNT) reinforced polylactic acid (PLA) (CNT/PLA) shape memory polymer (SMP) filaments used in fused deposition modeling were prepared at the Harbin Institute of Technology (HIT). The cross-sectional morphology of CNT/PLA filament (before the printing process) was characterized using Auriga 60 scanning electron microscope (SEM) with an accelerating voltage of 3.0 kV. The thermal gravimetric analysis (TGA) measurement of CNT/PLA filament was conducted in a Q600 TGA/DSC (TA Instruments) under nitrogen atmosphere from 20 °C to 600 °C with ramp rate of 10 °C/min. The sample weight was around 9 mg. The differential scanning calorimetry (DSC) measurement of CNT/PLA filament was also performed using a Discovery DSC (TA Instruments) from 20 °C to 200 °C with ramp rate of 10 °C/min. The sample weight was 4.2 mg. The thermal properties of PLA filament had been characterized in our previous work [12].

2.2. Preform and composite specimen fabrication

The angle-ply laminated and rectangular braided preforms were printed by fused deposition modeling (FDM) using both PLA and CNT/PLA shape memory polymer filaments. The angle-ply laminate was composed of nineteen –45° and 45° layers with mid-plane symmetry. The microstructure model of the rectangular braided preform with braiding angle of 45° was established by the CATIA software. The size of all specimens was around 60 mm (length) × 11 mm (width) × 5 mm (thickness). The yarn volume fraction of the rectangular braided preform was around 38%. The yarn volume fraction of the angle-ply laminate was also 38%, which was set on the 3D printer. It should be noted that the term “yarn” is used hereafter to describe the filament deposited by 3D printing. Besides using the established term in textile engineering, it is also intended to signify the fact that, unlike in traditional fiber composites, the size, shape and microstructure of yarns from fused deposition are not exactly the same as those of the pristine filament. The printing was conducted on a QIDI Tech 3D printer (Qidi Technology Co., China). The printer nozzle temperature of 200 °C and the printing speed of 50 mm/s were chosen. Furthermore, the Dow Corning 184 silicone elastomer system (Dow Corning Inc., Michigan, U.S.) was adopted to infuse the angle-ply laminate and braided preform for fabricating the composites (i.e., silicone matrix infusion process). Vacuum was applied to remove the air in the silicone elastomer matrix. The composites were cured at room temperature for 72 h to avoid the influence of heating on the shape memory polymer performance.

2.3. X-ray micro-computed tomography characterization

The microstructural imaging of 4D printed specimens was conducted using a Scanco μ CT35 scanner (Scanco Medical, Switzerland). The X-ray voltage and current were set to 70 kV and 57 μ A, respectively. The scanning resolution was around 18.5 μ m/pixel. In order to reduce the micro-CT imaging time, the lengths of as-printed specimens were cut to around 15 mm and the lengths of post-bending specimens for failure observation were cut to around 18 mm. The brightness and contrast of the acquired 2D images were modified using the CTvox software. 3D model reconstruction and cross-sectioning were also conducted using the CTvox software.

2.4. Characterization of shape recovery ratio and recovery force

The shape memory PLA used in our work is a kind of semi-crystalline polymer, in which both amorphous and crystalline regions exist in the polymer chains. This molecular network conforms to the two-phase structure required by shape memory effect. In the shape memory behavior of PLA, the phase transition temperature in the crystalline region is higher, which can be used as a stationary phase to memorize the initial shape of PLA. The molecular chains in the amorphous region are reversible phases and play a role in the transition between the temporary and initial shape of PLA. Shape recovery ratio and recovery force are the key characterizations of shape memory properties of the 4D printed preforms and their composites. The shape recovery ratio was measured based on the specimen free-shape memory. The schematic of a typical specimen shape recovery cycle is shown in Fig. 1a. The specimen was first uniformly heated at the high temperature T_h (higher than the glass transition temperature), in an oven and deformed into an intermediate L-shape under a bending load. The intermediate shape was maintained when the specimen was cooled down to an intermediate temperature, T_i , and unloaded. Upon heating to the temperature T_h again, the specimen without external load nearly recovered to its original shape. During the shape recovery cycle, T_h and T_i were chosen to be 90 °C and room temperature, respectively. The bending radius R_1 of around 8 mm was controlled by a mold. The evolution of shape recovery was recorded using a video camera (Sony FDR-AX100). The start of the recovery process was defined as the instant when a specimen was

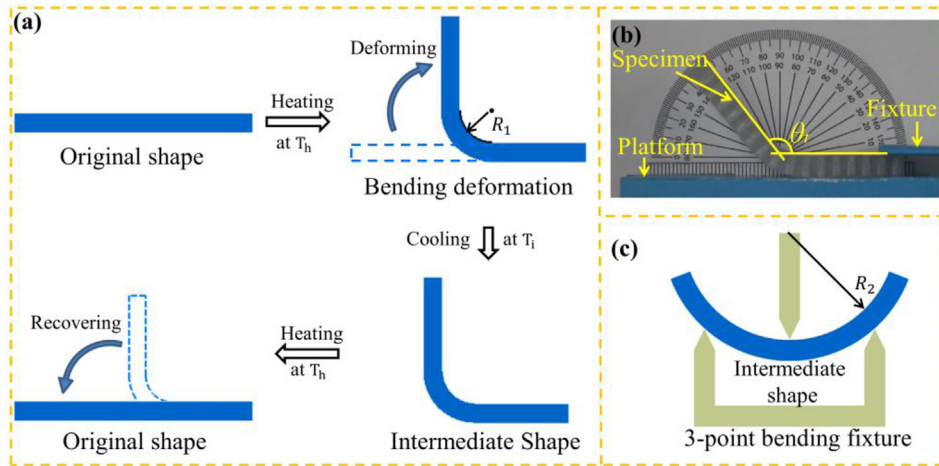


Fig. 1. Characterization methods of shape recovery ratio and recovery force. (a) Schematic of shape recovery cycle of a specimen. (b) Illustration of the Definition of the specimen angle θ_t at recovery time t . (c) Schematic of the recovery force characterization of a specimen using a DMA 3-point bending fixture.

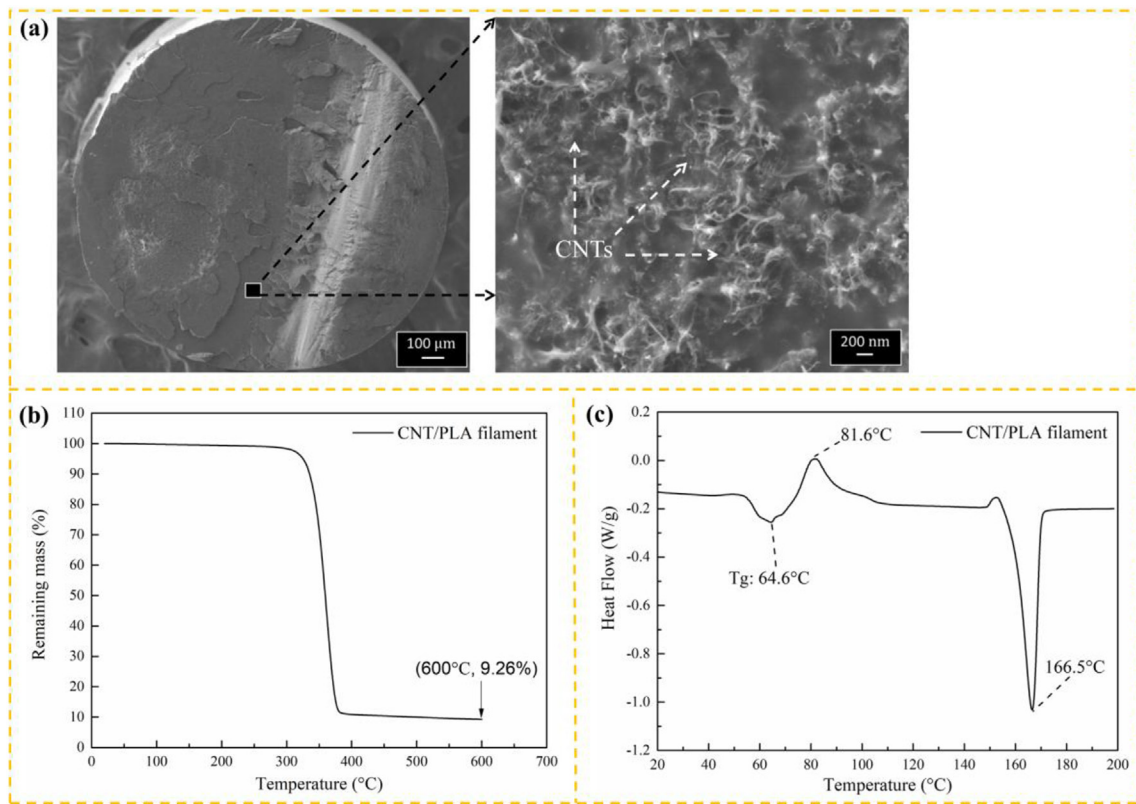


Fig. 2. Characterization of the CNT/PLA filament. (a) SEM cross-sectional morphology (left) and its partially enlarged SEM image (right). (b) TGA curve. (c) DSC curve.

placed in an oven at 90 °C, and the end of recovery process was defined as the time when the specimen shape was nearly unchanged during further heating. The shape recovery ratio (R_t) corresponding to the shape recovery time t can be calculated using the following definition:

$$R_t(\%) = (\theta_t - \theta_i) / (\theta_o - \theta_i) \times 100 \quad (1)$$

Here, θ_o , θ_t and θ_i denote the bending angles of the specimen shape at recovery time t , the intermediate state and the original state, respectively. The angle θ_t was defined by the specimen top surface (Fig. 1b) and measured using the image processing and analysis software (*ImageJ*, available on: <http://imagej.nih.gov/ij/>). The angles θ_i and θ_o were around 90° and 180°, respectively.

The recovery force was measured based on the specimen constrained-shape memory. The specimen was heated at 90 °C in an oven and bent to an intermediate shape. The intermediate shape with a radius of curvature $R_2 = 25$ mm was controlled and maintained with a pair of molds when it was cooled down to room temperature. A schematic of the characterization method for recovery force is shown in Fig. 1c. The characterization of recovery force of the deformed specimen was conducted using DMA (RSA-G2, TA Instruments) with a bending oscillatory temperature ramp from 25 °C to 90 °C at the ramp rate of 5 °C/min. The DMA instrument was chosen to do the recovery force measurements due to its force resolution of 0.00001 N and the three-point bending setup similar to that in usual thermomechanical

analysis instruments. A pre-load force around 0.01 N was applied to ensure the contact between the top of the fixture and the specimen. The oscillatory frequency was 1 Hz and the oscillatory strain was set to be 0.15%; these conditions were similarly to those adopted in other works [45,46]. It should be noted that the force measured by the DMA instrument with oscillatory condition consists of the force responding to 0.15% oscillatory strain and the true recovery force. The oscillatory strain of 0.15% with respect to the specimen thickness of 5 mm gave rise to the fairly small oscillatory amplitude of 7.5 μm , which is considered negligible. Therefore, the force measured by the DMA instrument very closely approximates the “true” recovery force.

2.5. Flexural property characterization

The flexural property measurements of 4D printed preforms and their silicone elastomer matrix composites have been conducted using 3-point bending tests with an Instron 5848 instrument, following the ASTM standard D7264/D7264M-15. The support span was 40 mm and the speed of deformation was 1 mm/min. The load and displacement were obtained. The fracture morphology of specimens was also examined using an X-ray $\mu\text{-CT}$ imaging.

3. Results and discussion

3.1. SEM morphology and thermal properties of CNT/PLA filament

The SEM cross-sectional micrographs of the CNT/PLA filament are shown in Fig. 2a. It can be seen that the CNTs are uniformly distributed in the filament cross-section. The TGA measurement of CNT/PLA filament was performed from 20 °C to 600 °C and the result is given in Fig. 2b. It shows that the remaining mass of the CNT/PLA filament was almost unchanged around 600 °C and the weight fraction of CNT in the filament was around 9.26%. Fig. 2c shows the DSC curve of the CNT/PLA filament. The glass transition temperature (T_g), the crystallization temperature and the melting temperature (T_m) of the CNT/PLA filament were around 64.6 °C, 81.6 °C and 166.5 °C, respectively. The T_g and T_m of the PLA filament were around 64.2 °C and 168.5 °C, respectively [12]. Based on the thermal properties of the filament, the nozzle temperature in the 3D printing process was set to be 200 °C.

3.2. Microstructure characterization of as-printed preforms

The microstructure design and $\mu\text{-CT}$ imaging characterization of the 4D printed angle-ply laminated and rectangular braided preforms are performed for both PLA and CNT/PLA specimens. Illustration of raster angles, 3D model, as-printed preform and $\mu\text{-CT}$ image of the PLA $\pm 45^\circ$ angle-ply laminate are given in Fig. 3a. The $\mu\text{-CT}$ image shows the high quality of the as-fabricated preform. The sectional $\mu\text{-CT}$ images of the PLA laminate (Fig. 3c) and CNT/PLA laminate (Fig. 3d) show highly ordered microstructures. Following the terminologies of textile engineering, the microstructure model of the rectangular braided preform was composed of three distinct parts: the interior yarns, surface yarns and corner yarns (Fig. 3b). The $\mu\text{-CT}$ images of the PLA braided preform (Fig. 3b) and the CNT/PLA braided preform (Fig. 3e) again demonstrated the good model-to-part fidelity of the preforms.

3.3. Characterization of shape memory behavior

To study the shape memory behavior, the time variations of shape recovery ratios of 4D printed specimens have been measured. As seen in Fig. 4a, these S-shaped curves show three stages of variations of recovery ratio with time, which is referred to herein as the shape recovery rate. At an identical time, the shape recovery ratios of the PLA and CNT/PLA braided preforms were larger than those of the PLA and CNT/PLA angle-ply laminated preforms, respectively. As compared to the 4D printed PLA specimens, the 4D printed CNT/PLA specimens had an

earlier start of recovery, slower shape recovery rate and smaller final shape recovery ratio. The final shape recovery ratios of the CNT/PLA laminated preform and braided preform were 81.3% and 85.3%, respectively. Fig. 4b shows the shape recovery ratio vs. time curves of 4D printed laminated preform/silicone matrix and braided preform/silicone matrix composites. It can be seen that the composites took longer time to start the recovery than the preforms. This can be attributed to the fact that the silicone matrix reduced the heat conduction. However, the times of final recovery of the composites were close to those of the un-infused specimens. Furthermore, at a given time, the shape recovery ratios of the CNT/PLA preform/silicone matrix composites were larger than those of the PLA preform/silicone matrix composites. The final shape recovery ratios of the CNT/PLA/silicone matrix laminated composite and braided composites were 97.3% and 96.6%, which were larger than those of the corresponding un-infused specimens. These results could be attributed to the fact that during the shape recovery process, the CNT/PLA preform was softened and the elastic strain energy of the silicone elastomer matrix was released, resulting in higher final recovery ratio. In other words, the CNT/PLA contributed to the shape memory effect while the elasticity of the silicone matrix contributed to the enhancement of the shape memory property of the CNT/PLA preform. Fig. 4c–e shows the shape recovery processes of 4D printed PLA braided preform, CNT/PLA braided preform and CNT/PLA braided preform/silicone matrix composite, respectively. At 40 s, the shape of 4D printed PLA braided preform just started to recover (Fig. 4c) while the shape of the CNT/PLA braided preform had an obvious recovery (Fig. 4d). At 80 s, the shape recovery degree of the CNT/PLA braided preform/silicone matrix composite was less than that of the CNT/PLA braided preform (Fig. 4d–e). The CNT/PLA braided preform/silicone matrix composite almost recovered to its original shape at 129 s while the recovery of CNT/PLA braided preform lagged behind. The shape recovery process images of other 4D printed specimens were shown in Fig. S1.

3.4. Characterization of shape recovery force

In order to further understand the effects of preform microstructure, CNT filler and silicone elastomer matrix on shape recovery capacity of the 4D printed preforms and their composites, recovery forces were characterized using DMA 3-point bending oscillatory temperature ramp from 25 °C to 90 °C. The recovery force, $\text{Tan}(\delta)$ and storage modulus vs. temperature curves of 4D printed CNT/PLA braided preform and its silicone matrix composite are chosen as two typical examples for discussion (Fig. 5a–b). It can be seen in the curves of the printed braided preform (Fig. 5a) that the $\text{Tan}(\delta)$ has a peak value at 64 °C, which is close to the glass transition temperature of the CNT/PLA filament characterized by DSC. The response to oscillatory strain dominated the force from 25 °C to 57 °C since the specimen did not have obvious recovery behavior as temperature below T_g . The increase in recovery force from 25 °C to 41 °C may be attributed to the specimen thermal expansion. The recovery force rapidly decreased to 0.18 N from 41 °C to 57 °C. As temperature above 57 °C, the specimen started to recover and the recovery behavior governed the force measured by DMA instrument. This could be verified by the fact that the recovery force increased from 57 °C to 64 °C while the storage modulus rapidly decreased. Above 64 °C, the recovery force stayed at a stable level of around 0.22N and then decreased due to the continuous decrease in storage modulus. The variation of thermomechanical properties of the CNT/PLA braided preform/silicone matrix composite are shown in Fig. 5b. It can be observed that the $\text{Tan}(\delta)$ approached the peak value at 63 °C, which is close to that of the braided preform. The recovery force at 25 °C is less than that of the braided preform, which can be attributed to the infusion of the silicone elastomer matrix. The recovery behavior of the CNT/PLA braided preform/silicone matrix composite from 25 °C to 57 °C was different from that of the preform due to the support of the silicone matrix. From 57 °C to 90 °C, the

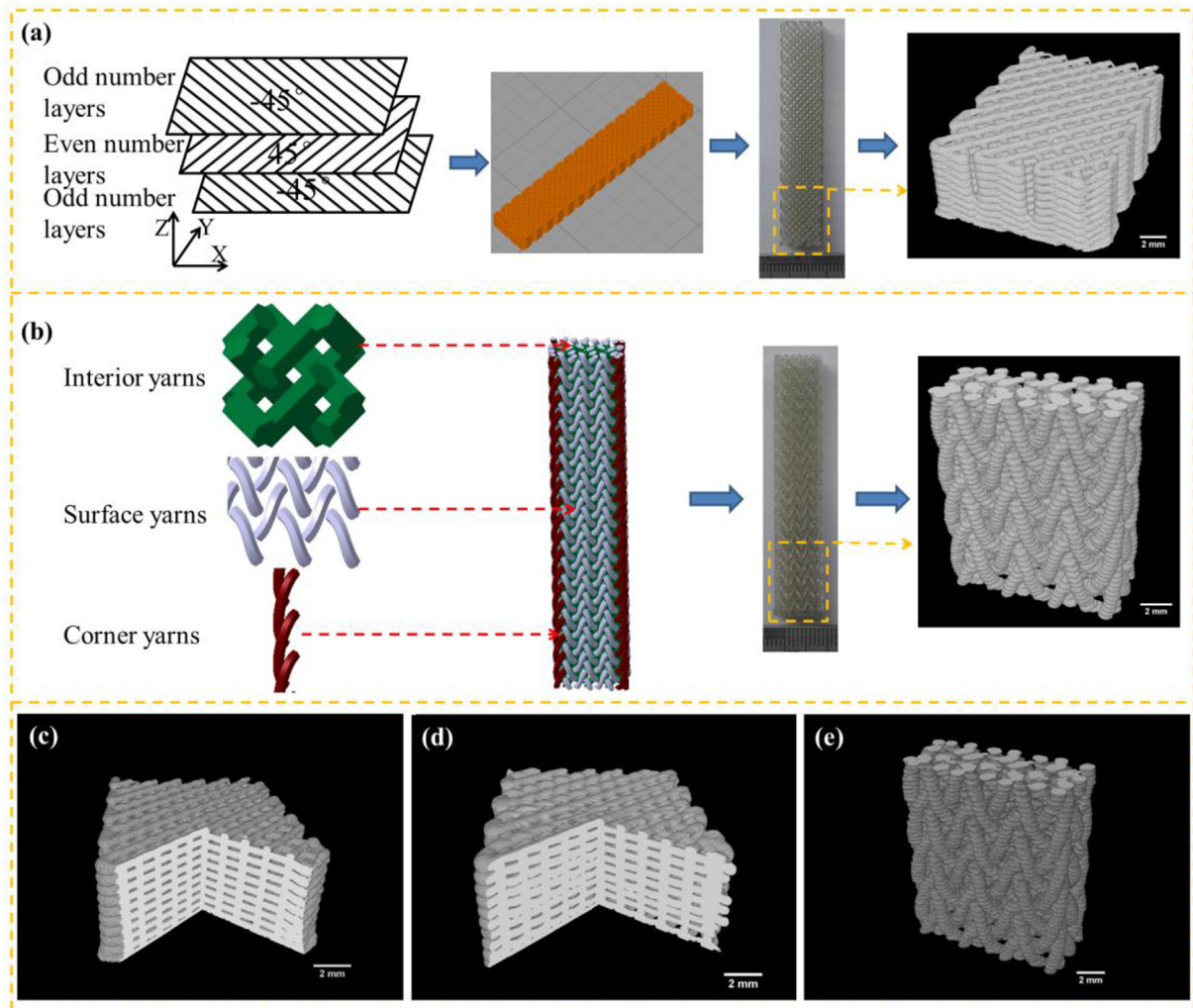


Fig. 3. Microstructural design and μ -CT imaging of 4D printed preforms. (a) Illustration of raster angles, 3D model, as-printed specimen and μ -CT image of the $\pm 45^\circ$ angle-ply laminated preform. (b) Representative units (interior yarns, surface yarns and corner yarns), 3D model, as-printed specimen and μ -CT image of the PLA rectangular braided preform with braiding angle of 45° . Sectional μ -CT images of (c) PLA $\pm 45^\circ$ angle-ply laminate and (d) CNT/PLA $\pm 45^\circ$ angle-ply laminate. (e) μ -CT image of the CNT/PLA 45° braided preform.

recovery force first increased and then decreased, approaching a peak load of 0.95 N at 63.6°C (close to T_g). The remarkable improvement in recovery force could be attributed to the fact that the elastic recovery force of the silicone matrix dominated the recovery force of the composite above 57°C .

Fig. 5c shows the recovery force vs. temperature curves of 4D printed angle-ply laminated preform and braided preform based on PLA and CNT/PLA filaments. The recovery forces of the PLA and CNT/PLA laminated preforms were larger than those of the PLA and CNT/PLA braided preforms, respectively. Due to the reinforcement of CNT filler, the recovery forces of the 4D printed CNT/PLA angle-ply laminated preform and braided preform were larger than those of 4D printed PLA angle-ply laminated preform and braided preform, respectively. For instance, at 65°C (close to T_g), the recovery force of the CNT/PLA laminated preform increased 123% and the recovery force of the CNT/PLA braided preform increased 144% as compared to those of their unreinforced PLA counterparts. Fig. 5d shows the recovery force vs. temperature curves of 4D printed angle-ply laminated preform/silicone matrix and braided preform/silicone matrix composites. The peak values of recovery forces of the four silicone matrix infused composites (Fig. 5d) were obviously larger than those of the corresponding preforms (Fig. 5c). The recovery forces of both CNT reinforced composites were higher than those without CNT reinforcement (Fig. 5d). The peak

load of CNT/PLA angle-ply laminated preform/silicone matrix composite showed the largest value of 1.28 N among all composites.

3.5. Flexural property and damage mode

The flexural behavior of 4D printed angle-ply laminated preform and rectangular braided preform and their composites was studied using 3-point bending measurement. Fig. 6a shows that the 4D printed PLA angle-ply laminated preform sustained larger bending load and displacement at failure than those of the PLA braided preform. The corresponding images of points 1, 2 and 3 on the load-displacement curve of the PLA laminated preform are shown in the insets of Fig. 6a. The PLA angle-ply laminate continued to carry partial loading after reaching the peak load and the load-bearing capacity at the displacement of 15 mm was 64.9% of the peak load. The flat portion of the curve of the braided preform indicated its good damage tolerance. Fig. 6b shows the load-displacement curves of the PLA and CNT/PLA printed angle-ply laminated preforms and their composites. The peak load of the CNT/PLA angle-ply laminated preform was 28.5% larger comparing to that of the PLA angle-ply laminated preform. Due to the infusion of silicone elastomer matrix, the peak loads of PLA and CNT/PLA angle-ply laminate/silicone matrix composites were larger than those of PLA and CNT/PLA angle-ply laminated preforms. The

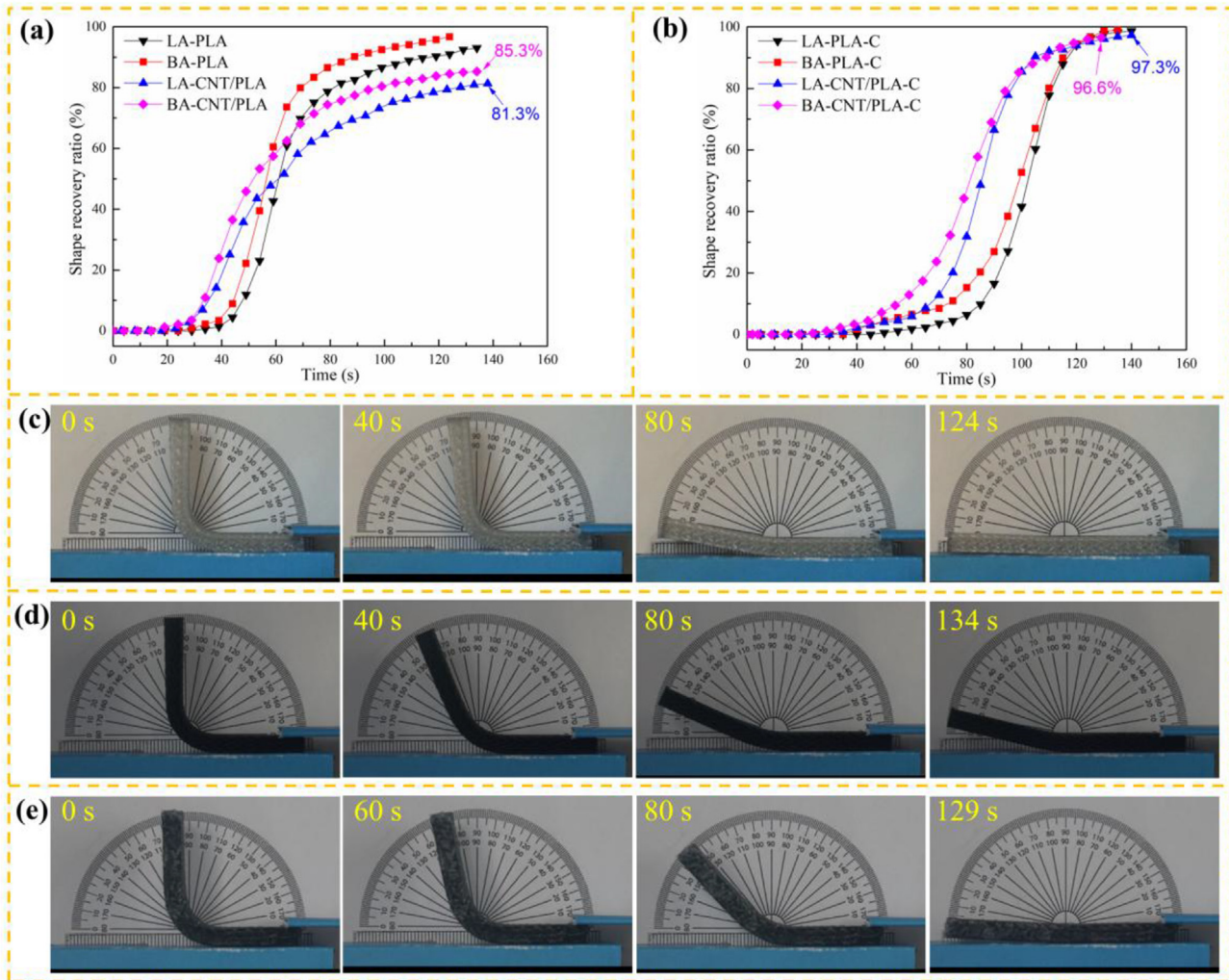


Fig. 4. Characterization of shape recovery ratio. Shape recovery ratio vs. time curves of (a) 4D printed PLA and CNT/PLA $\pm 45^\circ$ angle-ply laminated preform (LA) and rectangular braided (BA) preforms and (b) their silicone matrix composites. Shape recovery processes of (c) 4D printed PLA braided preform, (d) 4D printed CNT/PLA braided preform and (e) 4D printed CNT/PLA braided preform/silicone matrix composite uniformly heated in an oven at 90°C . (The legends LA and BA denote the angle-ply laminated and braided preforms, respectively. The legend without C denotes the preform and the legend with C means composite specimen. For example, the legend BA-CNT/PLA-C denotes the CNT/PLA braided preform/silicone matrix composite.)

displacements at ultimate failure of the CNT/PLA angle-ply laminated preform and its silicone matrix composite are smaller than those of the PLA counterparts. Fig. 6c shows the load-displacement curves of 4D printed PLA and CNT/PLA braided preform and their silicone matrix composites. The peak loads and ultimate failure displacements of the PLA and CNT/PLA braided preform/silicone matrix composites were larger than those of PLA and CNT/PLA braided preforms. This could be attributed to the effect of matrix strengthening through interfacial bonding. The peak load of the CNT/PLA braided preform improved 60.2% as compared to that of the PLA braided preform. The flexural modulus of the specimens is calculated by the equation [47].

$$E = \frac{sl^3}{4bh^3} \quad (2)$$

where s is the initial slope of the load-displacement curve, l is the fixture support span, b is the width and h is the thickness of the specimen. The flexural moduli of the specimens are shown in Fig. 6d. The flexural moduli of 4D printed CNT/PLA angle-ply laminated and braided preforms were remarkably larger than those of the corresponding PLA preforms. There were slight increases in the flexural moduli of the angle-ply laminated and braided preforms/silicone matrix composites as compared to the pure preforms.

The damage morphologies of the specimens were examined using μ -

CT imaging. The PLA angle-ply laminated preform had a ductile failure mode (Fig. 7a–b) while the CNT/PLA angle-ply laminated preform showed a more brittle failure mode (Fig. 7d–f). These results were consistent with the features of load-displacement curves shown in Fig. 6b. Furthermore, the 3D μ -CT image of Fig. 7c showed, the tensile and compressive load induced the interlayer yarn compaction and de-compaction, respectively. Fig. 7g–i show the optical image and μ -CT images of the 4D printed PLA braided preform. The non-simultaneous yarn fracture morphology may be responsible for the jagged load-displacement curve of the braided preform shown in Fig. 6c. The yarn breakage and interface de-bonding dominated the damage mode of the PLA braided preform. Fig. 7j–l shows the optical image and μ -CT images of 4D printed PLA braided preform/silicone elastomer matrix composite. As compared to those of the braided preform, the additional damage modes in the braided preform/silicone composite, such as matrix damage and yarn-matrix de-bonding (Fig. 7l), resulted in the larger peak load and ultimate failure displacement (Fig. 6c).

4. Conclusion

Micro-CT imaging, shape recovery behavior, recovery force as well as flexural property of 4D printed PLA and CNT/PLA angle-ply

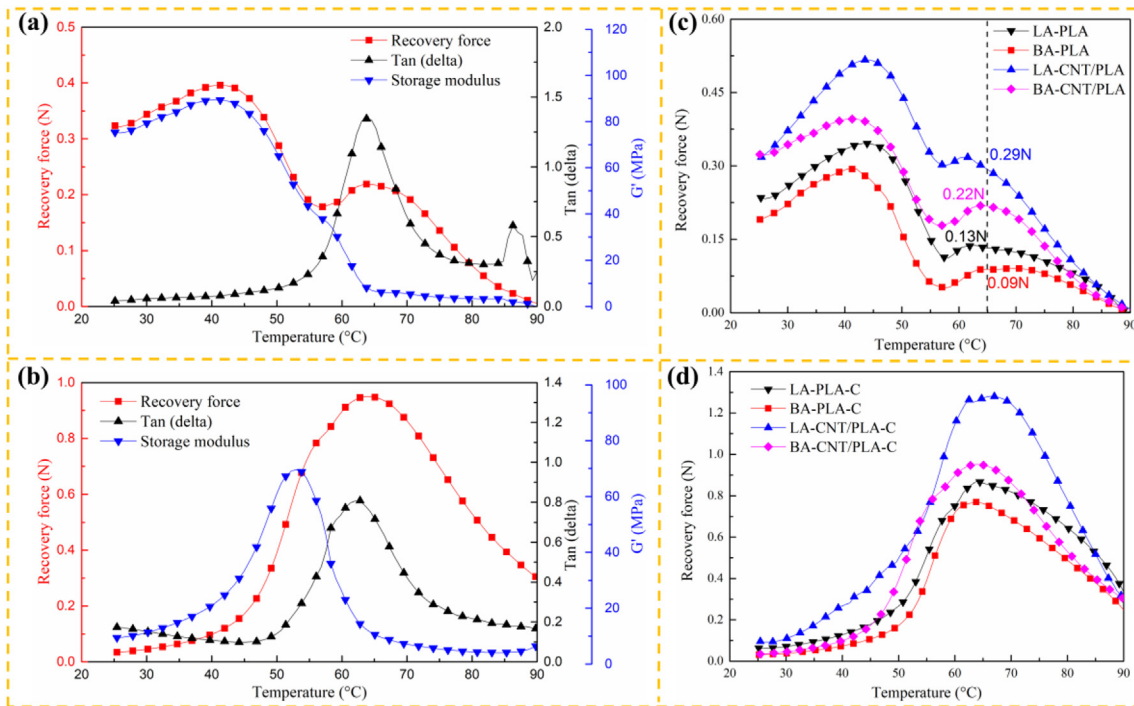


Fig. 5. Recovery force, Tan (delta) and storage modulus vs. temperature curves of (a) 4D printed CNT/PLA 45° rectangular braided preform and (b) its silicone matrix composite. Recovery force vs. temperature curves of (c) 4D printed ±45° angle-ply laminated preform and 45° braided preform based on PLA and CNT/PLA filaments and (d) their silicone matrix composites.

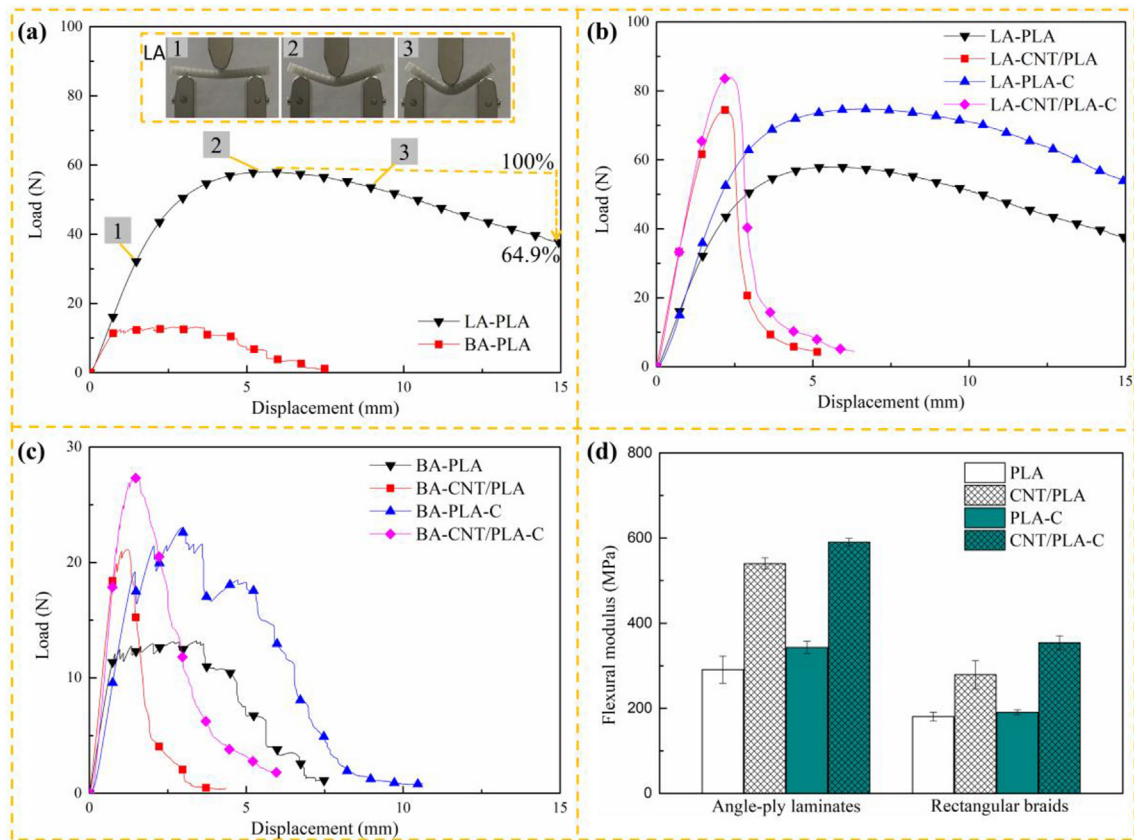


Fig. 6. Flexural characterization of 4D printed specimens subjected to 3-point bending load. Load vs. displacement curves of (a) 4D printed PLA angle-ply laminated preform and rectangular braided preform, (b) PLA and PLA/CNT angle-ply laminated preforms and their silicone matrix composites, (c) PLA and PLA/CNT rectangular braided preforms and their composites. (d) Flexural moduli of 4D printed preforms and their silicone matrix composites.

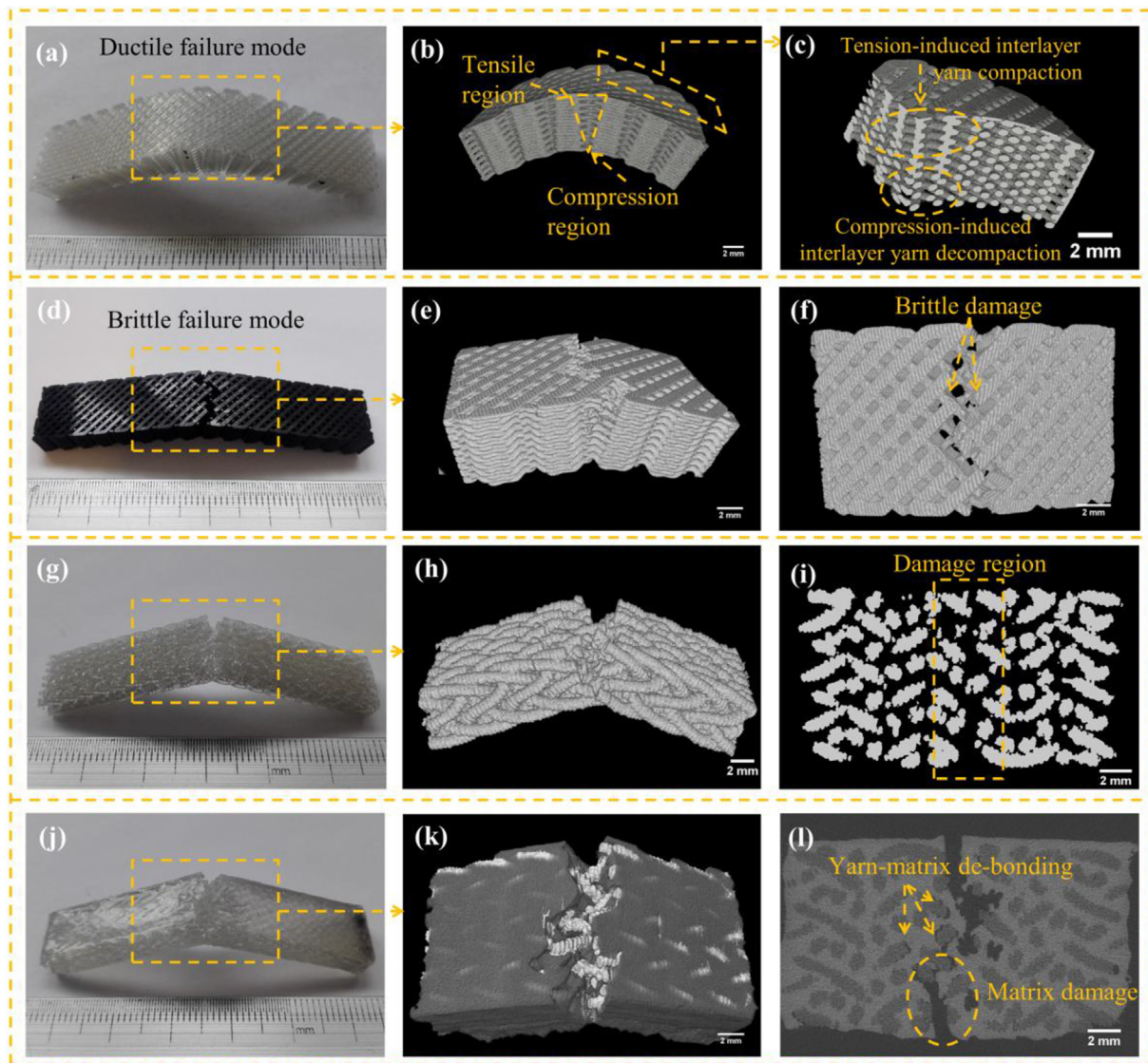


Fig. 7. Damage morphology of 4D printed specimens. PLA angle-ply laminated preform: (a) bending damage optical image, (b) 3D μ -CT image of damage region and (c) its quarter-cutting μ -CT image. CNT/PLA angle-ply laminated preform: (d) bending damage optical image, (e) oblique view and (f) top view of 3D μ -CT image of damage region. PLA braided preform: (g) bending damage optical image, (h) oblique view of 3D μ -CT image of damage region and (i) cross-section μ -CT image. PLA braided preform/silicone matrix composite: (j) bending damage optical image, (k) oblique view of 3D μ -CT image of damage region and (l) cross-section μ -CT image.

laminated and braided preforms and their silicone elastomer matrix composites have been characterized. Major findings of this work are summarized as follows.

- (1) The recovery force and flexural property of angle-ply laminated preforms and composites were superior to those of rectangular braided preforms and composites with the same yarn orientation (45°) and volume fraction (38%) while the shape recovery rate of angle-ply laminated preforms and composites were inferior to those of rectangular braided preforms and composites.
- (2) The infilling of CNT in the PLA printing filament enabled more rapid shape recovery of the specimens; the infusion of silicone elastomer matrix in the CNT/PLA angle-ply laminated and braided preforms enhanced the final shape recovery ratio of the resulting composites.
- (3) The additions of CNT and silicone matrix to the preforms markedly improved recovery force, flexural load and flexural modulus of the 4D printed composites.

The knowledge gained in this research will benefit future design

optimization for developing smarter, faster and stronger actuators.

Acknowledgements

Yang Liu acknowledges the financial support from the China Scholarship Council. Yang Liu also thanks Tao Liu for discussions on the model design of the braided preform and Shubo Wang for suggestions on flexural property test.

Appendix A. Supplementary data

Supplementary data to this article can be found online at <https://doi.org/10.1016/j.compscitech.2019.107692>.

References

- [1] Z. Quan, A. Wu, M. Keefe, X. Qin, J. Yu, J. Suhr, J.H. Byun, B.S. Kim, T.W. Chou, Additive manufacturing of multi-directional preforms for composites: opportunities and challenges, *Mater. Today* 18 (9) (2015) 503–512.
- [2] T.D. Ngo, A. Kashani, G. Imbalzano, K.T. Nguyen, D. Hui, Additive manufacturing (3D printing): a review of materials, methods, applications and challenges, *Compos.*

- B Eng. 143 (2018) 172–196.
- [3] S. Singh, S. Ramakrishna, R. Singh, Material issues in additive manufacturing: a review, *J. Manuf. Process.* 25 (2017) 185–200.
- [4] J. Leng, X. Lan, Y. Liu, S. Du, Shape-memory polymers and their composites: stimulus methods and applications, *Prog. Mater. Sci.* 56 (7) (2011) 1077–1135.
- [5] L. Sun, W.M. Huang, Z. Ding, Y. Zhao, C.C. Wang, H. Purnawali, C. Tang, Stimulus-responsive shape memory materials: a review, *Mater. Des.* 33 (2012) 577–640.
- [6] S. Tibbits, The Emergence of “4D Printing”, TED conference, 2013.
- [7] X. Kuang, D.J. Roach, J. Wu, C.M. Hamel, Z. Ding, T. Wang, M.L. Dunn, H.J. Qi, Advances in 4D printing: materials and applications, *Adv. Funct. Mater.* (2018), <https://doi.org/10.1002/adfm.201805290>.
- [8] F. Momeni, M.M.H.N. Seyed, X. Liu, J. Ni, A review of 4D printing, *Mater. Des.* 122 (2017) 42–79.
- [9] M. López-Valdeolivas, D. Liu, D.J. Broer, C. Sánchez-Somolinos, 4D printed actuators with soft-robotic functions, *Macromol. Rapid Commun.* 39 (5) (2018) 1700710.
- [10] Q. Ge, C.K. Dunn, H.J. Qi, M.L. Dunn, Active origami by 4D printing, *Smart Mater. Struct.* 23 (9) (2014) 094007.
- [11] G. Liu, Y. Zhao, G. Wu, J. Lu, Origami and 4D printing of elastomer-derived ceramic structures, *Sci. Adv.* 4 (8) (2018) eaat0641.
- [12] Y. Liu, W. Zhang, F. Zhang, X. Lan, J. Leng, S. Liu, X. Jia, C. Cotton, B. Sun, B. Gu, T.-W. Chou, Shape memory behavior and recovery force of 4D printed laminated Miura-origami structures subjected to compressive loading, *Compos. B Eng.* 153 (2018) 233–242.
- [13] Q. Zhang, K. Zhang, G. Hu, Smart three-dimensional lightweight structure triggered from a thin composite sheet via 3D printing technique, *Sci. Rep.* 6 (2016) 22431.
- [14] M. Bodaghi, A. Damanpack, W. Liao, Self-expanding/shrinking structures by 4D printing, *Smart Mater. Struct.* 25 (10) (2016) 105034.
- [15] B. Gao, Q. Yang, X. Zhao, G. Jin, Y. Ma, F. Xu, 4D bioprinting for biomedical applications, *Trends Biotechnol.* 34 (9) (2016) 746–756.
- [16] M. Zarek, M. Layani, S. Eliazar, N. Mansour, I. Cooperstein, E. Shukrun, A. Szlar, D. Cohn, S. Magdassi, 4D printing shape memory polymers for dynamic jewellery and fashionwear, *Virtual Phys. Prototyp.* 11 (4) (2016) 263–270.
- [17] Q. Ge, A.H. Sakhaei, H. Lee, C.K. Dunn, N.X. Fang, M.L. Dunn, Multimaterial 4D printing with tailorable shape memory polymers, *Sci. Rep.* 6 (2016) 31110.
- [18] M. Zarek, M. Layani, I. Cooperstein, E. Sachyani, D. Cohn, S. Magdassi, 3D printing of shape memory polymers for flexible electronic devices, *Adv. Mater.* 28 (22) (2016) 4449–4454.
- [19] Y.Y.C. Choong, S. Maleksaeedi, H. Eng, J. Wei, P.-C. Su, 4D printing of high performance shape memory polymer using stereolithography, *Mater. Des.* 126 (2017) 219–225.
- [20] J.E.M. Teoh, Y. Zhao, J. An, C.K. Chua, Y. Liu, Multi-stage responsive 4D printed smart structure through varying geometric thickness of shape memory polymer, *Smart Mater. Struct.* 26 (12) (2017) 125001.
- [21] S.E. Bakarich, R. Gorkin III, M.I.H. Panhuis, G.M. Spinks, 4D printing with mechanically robust, thermally actuating hydrogels, *Macromol. Rapid Commun.* 36 (12) (2015) 1211–1217.
- [22] Y.-C. Li, Y.S. Zhang, A. Akpek, S.R. Shin, A. Khademhosseini, 4D bioprinting: the next-generation technology for biofabrication enabled by stimuli-responsive materials, *Biofabrication* 9 (1) (2016) 012001.
- [23] C.P. Ambulo, J.J. Burroughs, J.M. Boothby, H. Kim, M.R. Shankar, T.H. Ware, Four-dimensional printing of liquid crystal elastomers, *ACS Appl. Mater. Interfaces* 9 (42) (2017) 37332–37339.
- [24] D.J. Roach, X. Kuang, C. Yuan, K. Chen, H.J. Qi, Novel ink for ambient condition printing of liquid crystal elastomers for 4D printing, *Smart Mater. Struct.* 27 (12) (2018) 125011.
- [25] W. Wang, C.Y. Yu, P.A.A. Serrano, S.-H. Ahn, Soft grasping mechanisms composed of shape memory polymer based self-bending units, *Compos. B Eng.* 164 (2019) 198–204.
- [26] M. Bodaghi, A. Damanpack, W. Liao, Adaptive metamaterials by functionally graded 4D printing, *Mater. Des.* 135 (2017) 26–36.
- [27] T. van Manen, S. Janbaz, A.A. Zadpoor, Programming 2D/3D shape-shifting with hobbyist 3D printers, *Mater. Horiz.* 4 (6) (2017) 1064–1069.
- [28] Z. Ding, C. Yuan, X. Peng, T. Wang, H.J. Qi, M.L. Dunn, Direct 4D printing via active composite materials, *Sci. Adv.* 3 (4) (2017) e1602890.
- [29] Z. Ding, O. Weeger, H.J. Qi, M.L. Dunn, 4D rods: 3D structures via programmable 1D composite rods, *Mater. Des.* 137 (2018) 256–265.
- [30] Q. Wang, X. Tian, L. Huang, D. Li, A.V. Malakhov, A.N. Polilov, Programmable morphing composites with embedded continuous fibers by 4D printing, *Mater. Des.* 155 (2018) 404–413.
- [31] J.-J. Wu, L.-M. Huang, Q. Zhao, T. Xie, 4D printing: history and recent progress, *Chin. J. Polym. Sci.* 36 (2018) 563–575.
- [32] T. Chen, K. Shea, An autonomous programmable actuator and shape reconfigurable structures using bistability and shape memory polymers, *3D Print. Addit. Manuf.* 5 (2018), <https://doi.org/10.1089/3dp.2017.0118>.
- [33] S. Akbari, A.H. Sakhaei, K. Kowsari, B. Yang, A. Serjoui, Z. Yuanfang, Q. Ge, Enhanced multimaterial 4D printing with active hinges, *Smart Mater. Struct.* 27 (6) (2018) 065027.
- [34] L. Chen, W. Li, Y. Liu, J. Leng, Epoxy shape-memory polymer reinforced by thermally reduced graphite oxide: influence of processing techniques, *J. Appl. Polym. Sci.* 132 (38) (2015) 42502.
- [35] X. Wang, J. Sparkman, J. Gou, Electrical actuation and shape memory behavior of polyurethane composites incorporated with printed carbon nanotube layers, *Compos. Sci. Technol.* 141 (2017) 8–15.
- [36] H. Xie, L. Li, X.-Y. Deng, C.-Y. Cheng, K.-K. Yang, Y.-Z. Wang, Reinforcement of shape-memory poly (ethylene-co-vinyl acetate) by carbon fibre to access robust recovery capability under resistant condition, *Compos. Sci. Technol.* 157 (2018) 202–208.
- [37] H. Chen, H. Xia, Y. Qiu, Q.-Q. Ni, Analyzing effects of interfaces on recovery rates of shape memory composites from the perspective of molecular motions, *Compos. Sci. Technol.* 163 (2018) 105–115.
- [38] B.L. Volk, D.C. Lagoudas, D.J. Maitland, Characterizing and modeling the free recovery and constrained recovery behavior of a polyurethane shape memory polymer, *Smart Mater. Struct.* 20 (9) (2011) 094004.
- [39] R. Bouaziz, F. Roger, K. Prashantha, Thermo-mechanical modeling of semi-crystalline thermoplastic shape memory polymer under large strain, *Smart Mater. Struct.* 26 (5) (2017) 055009.
- [40] H. Du, L. Liu, F. Zhang, W. Zhao, J. Leng, Y. Liu, Thermal-mechanical behavior of styrene-based shape memory polymer tubes, *Polym. Test.* 57 (2017) 119–125.
- [41] Z. Quan, Z. Larimore, A. Wu, J. Yu, X. Qin, M. Mirotznik, J. Suhr, J.-H. Byun, Y. Oh, T.-W. Chou, Microstructural design and additive manufacturing and characterization of 3D orthogonal short carbon fiber/acrylonitrile-butadiene-styrene preform and composite, *Compos. Sci. Technol.* 126 (2016) 139–148.
- [42] Z. Quan, Z. Larimore, X. Qin, J. Yu, M. Mirotznik, J.-H. Byun, Y. Oh, T.-W. Chou, Microstructural characterization of additively manufactured multi-directional preforms and composites via X-ray micro-computed tomography, *Compos. Sci. Technol.* 131 (2016) 48–60.
- [43] W. Zhang, A.S. Wu, J. Sun, Z. Quan, B. Gu, B. Sun, C. Cotton, D. Heider, T.-W. Chou, Characterization of residual stress and deformation in additively manufactured ABS polymer and composite specimens, *Compos. Sci. Technol.* 150 (2017) 102–110.
- [44] W. Zhang, C. Cotton, J. Sun, D. Heider, B. Gu, B. Sun, T.-W. Chou, Interfacial bonding strength of short carbon fiber/acrylonitrile-butadiene-styrene composites fabricated by fused deposition modeling, *Compos. B Eng.* 137 (2018) 51–59.
- [45] W. Zhang, F. Zhang, X. Lan, J. Leng, A.S. Wu, T.M. Bryson, C. Cotton, B. Gu, B. Sun, T.-W. Chou, Shape memory behavior and recovery force of 4D printed textile functional composites, *Compos. Sci. Technol.* 160 (2018) 224–230.
- [46] J.M. Hampikian, B.C. Heaton, F.C. Tong, Z. Zhang, C. Wong, Mechanical and radiographic properties of a shape memory polymer composite for intracranial aneurysm coils, *Mater. Sci. Eng. C* 26 (8) (2006) 1373–1379.
- [47] L. Wu, F. Zhang, B. Sun, B. Gu, Finite element analyses on three-point low-cyclic bending fatigue of 3-D braided composite materials at microstructure level, *Int. J. Mech. Sci.* 84 (2014) 41–53.